Onset of three-dimensionality in electromagnetically driven thin-layer flows

Douglas H. Kelley and Nicholas T. Ouellette[a)]
*Department of Mechanical Engineering and Materials Science, Yale University,
New Haven, Connecticut 06520, USA*

Two-dimensional fluid flow is often approximated in the laboratory with thin electromagnetically forced fluid layers. The faithfulness of such an experimental model must be considered carefully, however, because the physical world is inherently three-dimensional. By adapting an analysis technique developed for oceanographic data, we divide velocity measurements from a thin-layer flow into two components: one that is purely two-dimensional and another that accounts for all out-of-plane flow. We examine the two- and three-dimensional components separately, finding that motion in thin-layer flows is nearly two-dimensional at low Reynolds numbers, but that out-of-plane flow grows quickly above a critical Reynolds number. This onset is likely due to a shear instability. © *2011 American Institute of Physics*. [doi:10.1063/1.3570685]

I. INTRODUCTION

The physics of two-dimensional flow is rich in theory and application. Some behaviors that arise in two dimensions are unique, most famously the double cascade of energy and enstrophy.[1–3] Others are equivalent or analogous to three-dimensional phenomena, making two-dimensional studies valuable models for testing, development, and application of complex analytic tools.[4,5] Many behaviors manifested by two-dimensional flows are also important in the geostrophic flows in the oceans and atmosphere.[6] Moreover, rotating turbulence undergoes a continuous transition from three- to two-dimensionality as the rotation rate increases.[7] Hence, studying two-dimensional fluid flow can give insight into a variety of important scientific questions.

Accordingly, studies of two-dimensional flow have been undertaken in the laboratory. Laboratory experiments are valuable because they can quickly access a wide range of parameters, produce high-resolution data sets, and allow for complex boundary conditions. One common paradigm for such studies is the electromagnetically driven thin-layer flow, in which a thin layer of conductive fluid is placed in a magnetic field and stirred by the Lorentz forces that arise when a current is passed through the fluid.[8–19] Studying two-dimensional flow in a three-dimensional laboratory device, however, is necessarily an approximation. A key question for this model system is its faithfulness: how well do thin-layer flows approximate two-dimensionality?

A series of investigations has addressed the two-dimensionality of experimental thin-layer flows; for a summary see the recent review by Clercx and van Heijst.[20] Paret *et al.*[9] performed experiments with a lattice of vortices, comparing the decay time of the flow on the free surface of their system and on an internal layer. Their results suggested that, after an initial transient, the vertical velocity profile was consistent with Poiseuille flow, implying no velocity in the depth direction and therefore good two-dimensionality. Jüttner *et al.*[10] performed numerical simulations of two-dimensional flow with linear (Rayleigh) friction and found that when given a Poiseuille profile as an initial condition, the simulations agreed well with experiments, again suggesting good two-dimensionality. Satijn *et al.*,[12] however, performed explicitly three-dimensional simulations of decaying monopolar vortices and found that large layer depth and/or Reynolds number drove appreciable out-of-plane flow, which could be damped by stratification. More recently, Akkermans *et al.*[17–19] used three-dimensional numerical simulations and stereoscopic particle image velocimetry of decaying monopolar vortices to visualize the vertical motion directly. Those studies concluded that out-of-plane flows are driven primarily by the impermeability of the top and bottom boundaries and that the vertical profile is inconsistent with Poiseuille flow. Taken together, their results suggest that thin-layer flows approximate two-dimensionality only poorly, at least with the geometry and parameters they considered.

Here we present a laboratory study of the two-dimensionality of electromagnetically forced thin-layer flows. We use a similar forcing method and employ particle tracking in two dimensions to measure the in-plane velocity field with higher spatial resolution than previously achieved, tracking about 30 000 particles per frame. Adapting a technique developed for oceanographic data analysis,[21] we decompose the velocity of each particle into two components: one that is purely two-dimensional and is incompressible in the plane and one that accounts for all out-of-plane motion. This technique has not been previously applied to thin-layer flows and allows us to examine the two components separately, quantitatively assessing the characteristics and relative strength of the out-of-plane flow. We perform experiments spanning a range of Reynolds numbers not previously examined by any single study and find that the three-dimensional component is weak at low Reynolds numbers, but grows quickly above a critical Reynolds number $Re_c = 205$. This sharp onset is indicative of an instability and has not been observed previously.

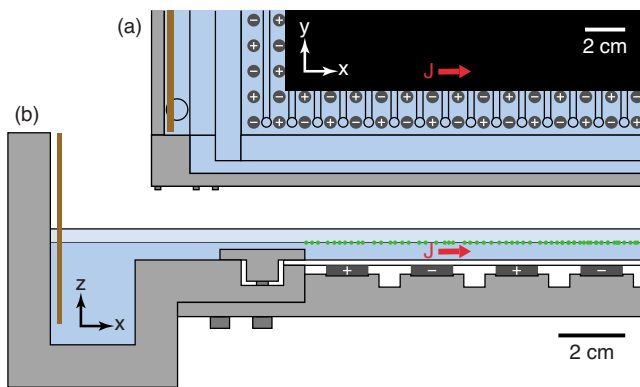a)Electronic mail: nicholas.ouellette@yale.edu.

23, 045103-1

FIG. 1. (Color online) The experimental apparatus. (a) Partial view from above, showing one electrode at left and a section of the magnet array. The polarity of each magnet is indicated with + or −, and a section of the floor encompassing the observation region is painted black to improve optical contrast. (b) Partial cross section, showing stably stratified layers of salt water and fresh water, with tracer particles (not drawn to scale) at their interface. Electric current with density J flows from left to right in the saltwater layer. The combination of current and magnetic fields leads to a Lorentz body force that drives fluid flow.

Below, we begin by presenting a description of our experimental apparatus and particle tracking techniques. We then describe the method by which we decompose the measured velocity of each particle into a purely two-dimensional component and a component that accounts for out-of-plane flow: we project experimental data onto basis modes built from a streamfunction and a velocity potential. We then present experimental results showing an abrupt onset of stronger three-dimensional flow at a critical Reynolds number. We close with a discussion of physical mechanisms that might be involved and a comparison of our results to those of previous studies.

II. EXPERIMENTAL FLOW AND PARTICLE TRACKING

Our apparatus (Fig. 1) consists of a thin layer of an electrolytic fluid with lateral dimensions of 86×86 cm^2. The experiments described below were performed with a 5 mm layer of 16% by mass NaCl in water, with a density of $\rho = 1116$ kg/m^3 and a kinematic viscosity of $\nu = 1.24 \times 10^{-6}$ m^2/s. The electrolyte is supported by a smooth flat glass floor, which is coated with hydrophobic wax to reduce friction and painted black on its underside to improve the visibility of tracer particles.

A square array of 34×34 cylindrical neodymium-iron-boron (NdFeB) grade N52 magnets lies beneath the glass floor. The magnets, with diameter of 12.7 mm and thickness of 3.2 mm, are spaced 25.4 mm on center with alternating polarity. Each magnet produces a field with a maximum amplitude of about 0.3 T that decays exponentially with the axial distance from the magnet surface, dropping to half the maximum in 3.3 mm.[22] A pair of bar electrodes are mounted on opposite ends of the layer, allowing an electric current to be passed through the salt water. The current and magnetic field produce a Lorentz body force $F = J \times B / \rho$, where J is the current density and B is the magnetic field, on the fluid that drives flow. The experiments presented were performed with steady (dc) forcing currents. At low current density J

$= |J|$, the forcing is weak and the flow generated is a steady lattice of vortices of spatially alternating sign. At higher currents, stronger forcing leads to time-dependent flows, spatiotemporal chaos, and eventually three-dimensional flow, as we will describe below. We characterize the flow by the Reynolds number, defined here as $Re = UL_f \nu^{-1}$, where $L_f = 25.4$ mm is the forcing scale and $U = \sqrt{\langle u^2 + v^2 \rangle}$ is the measured in-plane root-mean-square velocity, with brackets $\langle \cdot \rangle$ signifying a spatial average. We describe the flow as $u\hat{x} + v\hat{y} + w\hat{z}$ in a Cartesian coordinate system (x, y, z) with unit vectors $(\hat{x}, \hat{y}, \hat{z})$, respectively; $\hat{x}$ is the direction of the forcing current and $\hat{z}$ is the out-of-plane direction. We studied the range $30 \leq Re \leq 250$, a Reynolds-number range that lies between previous studies that have found three-dimensional effects to be negligible[9,10] and those that have found them to be important.[12,17–19]

To track the motion of the fluid, we add tracer particles to the fluid. The particles are 51 μm diameter fluorescent polystyrene spheres with density of 1050 kg/m^3. Because their density is less than that of the salt water, they float on its surface. If the upper surface of the salt water layer was an immiscible liquid-liquid interface or a gas-liquid interface, surface tension effects would lead to a long-range attractive force between the particles.[23] This interaction would lessen the ability of these particle to follow the flow by both modifying their equation of motion and by leading to clumping and therefore larger effective particle diameters.[24] We avoid this problem by placing a 5 mm layer of de-ionized water, which is less dense than the tracer particles, above the salt water. Because the two fluids are miscible, there is no bulk surface tension between them. When filling the apparatus, we add fresh water first and then inject salt water slowly from below to maintain the stable stratification and minimize mixing.

The fluorescent particles absorb most strongly in the blue (468 nm) and emit most strongly in the green (508 nm). We illuminate them with blue light emitting diodes with a luminosity that peaks at 470 nm and record images with an IDT MotionPro M5 camera fitted with a 24 mm focal length Schneider APO-Xenoplan lens. An optical filter attenuates wavelengths below 520 nm, reducing blue glare considerably while negligibly dimming the green particles. The camera has a complementary metal-oxide semiconductor sensor with pixel dimensions of 2320×1728 and can record continuously at frame rates of up to 170 Hz. The resulting movies are recorded to a parallel array of eight high-speed disks for later processing. The experiments discussed below were performed at a working distance of 40 cm, giving a field of view of 31.7×23.6 cm^2 in the center of the apparatus, well away from the walls. We recorded images at a rate of 60 Hz, which was sufficient to resolve the motion of even the fastest particles.

To measure the flow dynamics, we identify and follow the particles in recorded movies using Lagrangian particle tracking.[25] As is done in classical particle tracking velocimetry (PTV), we locate the positions of individual particles and match them in time. Unlike in PTV, however, which typically uses only two images to match particles, we keep the full Lagrangian information about the long-time particle

trajectories. Lagrangian dynamics are a powerful way to study fluid flow;[26] for the present application, the length of our trajectories is useful in that it allows us to use a numerical differentiation scheme that is more robust than simple finite differences.

Our tracking algorithm has been described in detail elsewhere,[25] and so here we summarize the major steps only briefly. Particles are located by using local maxima in image intensity (above a small threshold) and the pixels immediately adjacent to the maxima. We obtain the particle centers with a resolution of roughly 0.1 pixels (13.7 μm in these experiments) by fitting one-dimensional Gaussians to the $\hat{x}$- and $\hat{y}$-direction intensity profiles. Once the particle locations have been found, they are tracked using a predictive three-frame best-estimate algorithm. For each partially constructed trajectory, the expected position of the particle at the next time step is estimated using simple kinematics. The measured particle position that comes closest to this estimate is then chosen to continue the trajectory. Small temporal gaps (due to particle dropout) are bridged via extrapolation. The entire process has been shown to be robust under a wide range of flow conditions and has been parallelized so as to be computationally efficient. For the data reported here, we tracked $N_p \sim 30\,000$ particles per frame. We subsequently differentiate the trajectories temporally by convolving the measured tracks with a Gaussian smoothing and differentiating kernel,[27,28] yielding a time series of positions and velocities for each tracked particle.

III. DISTINGUISHING THE THREE-DIMENSIONAL COMPONENT WITH BASIS MODES

Our apparatus and others like it are used to approximate two-dimensional flow. In the three-dimensional physical world, however, they are only approximations, and thus there will also be some three-dimensional flow. The magnitude of the out-of-plane component can vary widely depending on experimental parameters. We have implemented an analytical technique to distinguish the three-dimensional component from the two-dimensional component in data where only in-plane velocity measurements are available. These components are not projections onto coordinate axes that are orthogonal in physical space but rather projections onto orthogonal basis functions that satisfy the appropriate boundary conditions. The basis set is composed of two types of modes, some purely two-dimensional and others that account for three-dimensionality. With this technique it is possible not only to measure the magnitude of the three-dimensional component (that is, the part of the flow contained in the three-dimensional basis modes), but to study its spatial and statistical properties separately from the two-dimensional component or to remove the three-dimensional component altogether. The remainder of this section describes the technique in detail.

Central to the technique is the relationship between out-of-plane motion and apparent in-plane compressibility. Because the Mach number in our flow is always $\mathcal{O}(10^{-5})$ or smaller, the flow is certainly incompressible in three dimensions, and so

$$\partial_x u + \partial_y v + \partial_z w = 0. \tag{1}$$

If the flow were truly two-dimensional, we would have $w = 0$ and therefore the flow would also satisfy incompressibility in the plane, given by

$$\boldsymbol{\nabla} \cdot \boldsymbol{u} = 0, \tag{2}$$

where $\boldsymbol{\nabla} = \hat{x}\partial_x + \hat{y}\partial_y$ is the two-dimensional gradient operator and $\boldsymbol{u} = u\hat{x} + v\hat{y}$ is the two-dimensional velocity field. In a real-world approximation of two-dimensional flow, Eq. (2) fails to hold whenever out-of-plane flow exists. Setting $\partial_x u = \partial_y v = 0$ in Eq. (1) yields $\partial_z w = 0$. Integrating that expression and using the boundary condition $w = 0$ at the impermeable floor show that the only solution compatible with apparent two-dimensional incompressibility is $w = 0$ *everywhere*. Apparent in-plane compressibility is an indicator of three-dimensionality.

The component that appears compressible can be separated from the incompressible component of the flow. According to the fundamental theorem of vector calculus (often called Helmholtz's theorem), if a smooth vector field is defined on some (possibly infinite) domain and if the amplitude of the field goes to zero at the boundaries, then the field can be uniquely represented as the sum of a solenoidal part and an irrotational part.[29] In particular, the theorem holds for any two-dimensional flow field $\boldsymbol{u}$, which can be written in terms of a streamfunction Ψ and a velocity potential χ, both scalar fields, such that

$$\boldsymbol{u} = -\hat{z} \times \boldsymbol{\nabla}\Psi + \boldsymbol{\nabla}\chi, \tag{3}$$

where $\hat{z} \times \boldsymbol{\nabla}$ is the two-dimensional curl operator. The first term on the right-hand side of Eq. (3) is solenoidal, whereas the second is irrotational, that is,

$$\boldsymbol{\nabla} \cdot (\hat{z} \times \boldsymbol{\nabla}\Psi) = 0,$$

$$\hat{z} \times \boldsymbol{\nabla}(\boldsymbol{\nabla}\chi) = 0. \tag{4}$$

Thus, the apparent compressibility associated with out-of-plane flow is contained entirely in the velocity potential.

One detail, however, remains. This decomposition is not precisely applicable to data sets typically recorded in experimental devices of this sort because Helmholtz's theorem requires that the vector field under consideration vanishes at the boundaries of the domain on which it is defined. Because the sidewalls of the apparatus lie outside the field of view of the camera, our recorded velocity fields do not drop to zero at the boundaries of the field of view. With "open boundaries" of this sort, decomposition into incompressible and irrotational components remains possible but is no longer unique.[30] Rather, the results of decomposition depend on the boundary conditions. Following Lekien et al.,[21] we use a unique three-part decomposition chosen to maximize the energy contained in the two-dimensional solenoidal flow field. We write the velocity as

$$\boldsymbol{u} = -\hat{z} \times \boldsymbol{\nabla}\Psi + \boldsymbol{\nabla}\Theta + \boldsymbol{\nabla}\Phi, \tag{5}$$

with the boundary conditions

$$\Psi|_\Gamma = 0,$$

$$\hat{\boldsymbol{n}} \cdot \boldsymbol{\nabla}\Theta|_\Gamma = g(s),$$

$$\hat{\boldsymbol{n}} \cdot \boldsymbol{\nabla}\Phi|_\Gamma = 0. \tag{6}$$

Here we denote the open boundary as Γ and the unit normal to the boundary as $\hat{\boldsymbol{n}}$. The scalar function $g(s)$, which depends on the arc length s of the boundary, will be addressed below. Θ and Φ together take the place of χ. The term $\boldsymbol{\nabla}\Theta$ gives the inflow and outflow at the boundaries and is both irrotational [see Eq. (4)] and solenoidal because

$$\boldsymbol{\nabla} \cdot (\boldsymbol{\nabla}\Theta) = 0. \tag{7}$$

Therefore, the term $\boldsymbol{\nabla}\Phi$ accounts for all apparent compressibility—and therefore all three-dimensionality—in the flow.

In order to decompose our experimental data according to Eq. (5), we first write each part of the flow as an expansion in orthogonal modes,

$$\Psi(x,y) = \sum_{j=1}^{N_\psi} \alpha_j \psi_j(x,y),$$

$$\Theta(x,y) = \sum_{k=1}^{N_\theta} \beta_k \theta_k(x,y),$$

$$\Phi(x,y) = \sum_{l=1}^{N_\phi} \gamma_l \phi_l(x,y), \tag{8}$$

with (so far undetermined) coefficients α_j, β_k, and γ_l; N_ψ, N_θ, and N_ϕ give the number of modes for each component. We refer to ψ_j, θ_k, and ϕ_l as streamfunction, boundary, and potential modes, respectively. In our experimental measurements, the kinetic energy associated with boundary modes has varied between 2% and 18% of the total kinetic energy, which quantifies the error introduced by ignoring them and using a two-part decomposition instead (see below). Combining Eqs. (5) and (8) we can write

$$u = \sum_{j=1}^{N_\psi} \alpha_j \partial_y \psi_j + \sum_{k=1}^{N_\theta} \beta_k \partial_x \theta_k + \sum_{l=1}^{N_\phi} \gamma_l \partial_x \phi_l,$$

$$v = -\sum_{j=1}^{N_\psi} \alpha_j \partial_x \psi_j + \sum_{k=1}^{N_\theta} \beta_k \partial_y \theta_k + \sum_{l=1}^{N_\phi} \gamma_l \partial_y \phi_l, \tag{9}$$

which give two-dimensional basis sets onto which measurements can be projected. The coefficients in each sum are set by the experimental measurements using a linear least-squares method, discussed further below. For notational simplicity, we define the full set of basis functions (including contributions from all three parts) as

$$u_m = \{\partial_y \psi_j\} \cup \{\partial_x \theta_k\} \cup \{\partial_x \phi_l\},$$

$$v_m = \{-\partial_x \psi_j\} \cup \{\partial_y \theta_k\} \cup \{\partial_y \phi_l\} \tag{10}$$

and the full set of coefficients as $\eta_m = \{\alpha_j\} \cup \{\beta_k\} \cup \{\gamma_l\}$. Then, Eq. (9) can be rewritten concisely as

$$u = \sum_{m=1}^{N} \eta_m u_m,$$

$$v = \sum_{m=1}^{N} \eta_m v_m, \tag{11}$$

where $N = N_\psi + N_\theta + N_\phi$. Choosing $N_\psi = N_\theta = N_\phi = \infty$ allows the, in principle, exact representation of any flow with open boundaries, but in practical situations it is necessary to truncate the series by choosing N_ψ, N_θ, and N_ϕ to be finite, as we will discuss further below. The exact forms of ψ_j, θ_k, and ϕ_l will also be specified below.

Equation (11) shows that u and v are determined by the same coefficients η_m. The best-fit projection of the data onto this model (in a least-squares sense) is given by the solution of the matrix equations[31]

$$\sum_{p=1}^{N_p} \sum_{m=1}^{N} (u_{mp} u_{np} + v_{mp} v_{np}) \eta_m = \sum_{p=1}^{N_p} (u_{np} u_p^{\text{meas}} + v_{np} v_p^{\text{meas}}), \tag{12}$$

known as the normal equations of the linear least-squares fit. Here p indexes the N_p particles present in the frame, and all sums are written explicitly. The notation u_{mp} signifies the value of the basis mode u_m, as defined in Eq. (10), evaluated at the location of particle p; u_{np}, v_{mp}, and v_{np} have corresponding meanings. Likewise u_p^{meas} and v_p^{meas} are the components of the velocity as measured for particle p.

We use singular value decomposition to solve Eq. (12) in order to avoid numerical issues that may arise due to nearly singular matrices and due to basis modes that are nearly degenerate at the particle locations where measurements have been recorded.[31] Once the coefficients η_m are known, the velocity vector components u and v can be reconstructed by simply summing over the basis modes as given by Eq. (11).

We must therefore specify the form of the modes ψ_j, θ_k, and ϕ_l explicitly. To construct the streamfunction modes ψ_j, we use the eigenfunctions of the Laplacian given by

$$\nabla^2 \psi_j = \lambda_j^\psi \psi_j, \tag{13}$$

where λ_j^ψ is the eigenvalue associated with the eigenfunction ψ_j, subject to the boundary conditions given by Eq. (6). Eigenfunctions of the Laplacian are used in many situations where an orthogonal complete set is required. Their exact form varies with the geometry and the boundary conditions; examples include scalar and vector spherical harmonics and Bessel functions. For a scalar field (such as the streamfunction Ψ) on a two-dimensional rectangular domain, the eigenfunctions of the Laplacian are two-dimensional Fourier modes. They cannot be specified analytically for an irregular domain such as the one defined by our tracer particles (note the irregular boundary in Fig. 3), but they can be calculated numerically, as we do for the data discussed below. Three streamfunction modes calculated this way are shown in Fig. 2. Some resemble Fourier modes closely (particularly for low orders), whereas others do not.

The boundary modes θ_k are determined entirely by the boundary conditions.[21] Because they are both irrotational and
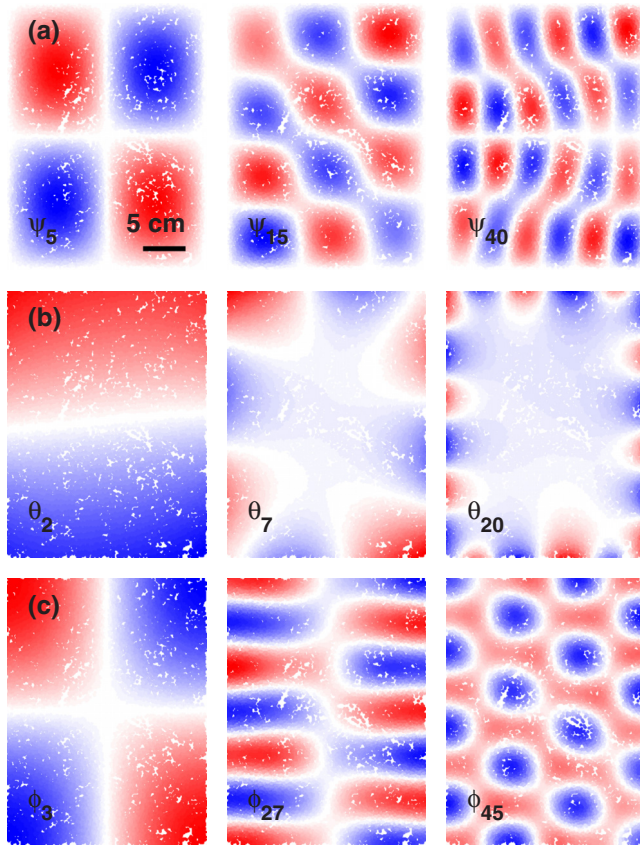
FIG. 2. (Color online) Example basis modes. (a) Three streamfunction modes ψ_j. A dot is drawn at the location of each tracked particle, much larger than the actual particle, with its color representing the value of the mode at that location; the overall amplitude is arbitrary. (b) Three boundary modes θ_k, drawn the same way. (c) Three velocity potential modes ϕ_l, drawn the same way. A superposition of basis modes such as these is used to represent each frame of measured data.

solenoidal, they are solutions of Laplace's equation. To specify the boundary conditions, let the local outflow at a point s on the boundary Γ be $G(s) = \hat{n} \cdot u$. We can then expand G in N_θ Fourier modes as

$$G(s) = \sum_{k=1}^{N_\theta} \mu_k g_k\left(\frac{\pi s}{L_b}\right),$$ (14)

where L_b is the total length of the boundary (so that $0 \leq s < L_b$) and

$$g_k(x) = \begin{cases} \sin kx, & k \text{ even} \\ \cos(k+1)x, & k \text{ odd.} \end{cases}$$ (15)

We choose the basis in this way so that each g_k is continuous over the boundary and

$$\int_0^{L_b} G(s)\,ds = \int_0^{L_b} g_k\left(\frac{\pi s}{L_b}\right)ds = 0,$$ (16)

as required by incompressibility. Defined in this way, the g_k provides a Neumann boundary condition on the Laplace equation that determines the boundary modes θ_k, so that the θ_k are given by

$$\nabla^2 \theta_k = 0,$$

$$\hat{n} \cdot \nabla \theta_k|_\Gamma = \left. g_k\left(\frac{\pi s}{L_b}\right)\right|_\Gamma.$$ (17)

Three boundary modes calculated this way are shown in Fig. 2.

We construct the potential modes ϕ_l in a similar way as the streamfunction modes, using numerically determined eigenfunctions of the Laplacian,

$$\nabla^2 \phi_l = \lambda_l^\phi \phi_l,$$ (18)

but with a different boundary condition, as given in Eq. (6). Here λ_l^ϕ is the eigenvalue associated with the eigenfunction ϕ_l. Three potential modes calculated this way are also shown in Fig. 2.

The number of modes to be used in projection must also be chosen. One consistent way to choose N_ψ, N_θ, and N_ϕ is by choosing a minimum size $L_{\min}$ and retaining all modes whose characteristic length scale exceeds that size. According to Eq. (15) we retain all boundary modes θ_k satisfying

$$\frac{2L_b}{k} \geq L_{\min}.$$ (19)

Because the streamfunction modes and potential modes are calculated numerically, their length scales are not immediately apparent but may be approximated with dimensional arguments. Following Lekien et al.,[21] we retain all streamfunction modes ψ_j satisfying

$$L_x \sqrt{\frac{\lambda_1^\psi}{\lambda_k^\psi}} \geq L_{\min},$$ (20)

where λ_1^ψ is the lowest streamfunction mode eigenvalue and L_x is the extent of the field of view in the $\hat{x}$-direction. Likewise we retain all potential modes ϕ_l satisfying

$$L_x \sqrt{\frac{\lambda_1^\phi}{\lambda_m^\phi}} \geq L_{\min},$$ (21)

where λ_1^ϕ is the lowest potential mode eigenvalue. In the experimental data described below, we have chosen $L_{\min} = L_f/2$. With that choice, we find that boundary modes account for about 2% of the kinetic energy of the flow. Increasing $L_{\min}$ does little to change the amount of energy captured by boundary modes; small-scale boundary modes capture little energy because their amplitudes are appreciable only in a narrow margin near the boundary. Small-scale internal modes, however, have appreciable amplitude everywhere; neglecting them by increasing $L_{\min}$ noticeably reduces the amount of energy captured by internal modes. Thus, boundary modes account for a larger fraction of the energy. Likewise, choosing a smaller region of interest increases the fraction of energy in boundary modes because more of the region lies in that narrow margin. In the special case of an open boundary through which no flow occurs, the boundary modes contain no energy, consistent with Helmholtz's theorem. On the other hand, choosing a boundary that maximizes inflow and outflow also maximizes the fraction of energy in boundary modes. In such an extreme case, we have seen boundary modes account for as much as 18% of the energy of the flow.
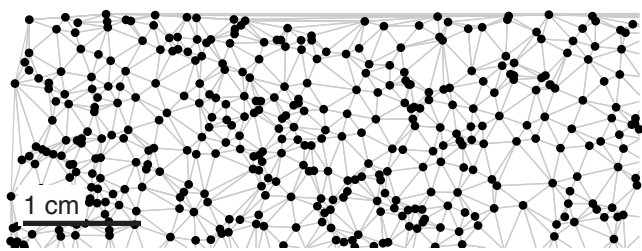
FIG. 3. A portion of an example particle mesh as seen from above. Particle locations are indicated by dots much larger than the actual size of the particles. The subregion shown contains 395 of the 29 047 particles identified and tracked in this particular frame. The mesh itself, computed from the particle locations via a Delaunay triangulation, connects the particles, with parts of its edge visible along the top and left. We use this mesh to calculate spatial derivatives of the velocity at the particle locations via finite-element techniques.

Evaluating Eq. (9) requires calculating spatial gradients. When data lie on a regular grid, spatial gradients are typically calculated using finite differences or similar techniques. However, Lagrangian particle tracking produces data that are not regularly spaced: measurements are made at the locations of the particles and nowhere else. We therefore calculate spatial gradients at the (essentially random) particle locations using finite-element tools. For each frame, we use Delaunay triangulation to build a mesh whose vertices are the particle locations and then calculate gradients using that triangular mesh. A typical mesh constructed this way is shown in Fig. 3.

IV. RESULTS

With a mechanism in place to separate the three-dimensional flow component from the purely two-dimensional component, we can address in detail the two-dimensionality of our electromagnetically forced thin-layer flow. By projecting the measured data using the technique described above, we can reconstruct the component that is incompressible in the plane (which we call simply the incompressible component) and the component that shows apparent compressibility (which we call the compressible component) separately; they are

$$\boldsymbol{u}_{\text{inc}} = -\hat{z} \times (\boldsymbol{\nabla}\Psi + \boldsymbol{\nabla}\Theta), \tag{22}$$

$$\boldsymbol{u}_{\text{comp}} = \boldsymbol{\nabla}\Phi, \tag{23}$$

respectively, where again $\hat{z} \times \boldsymbol{\nabla}$ is the two-dimensional curl operator.

When the forcing current is small and Re is low, we observe a flow field that closely aligns with the regular lattice of the magnetic forcing, as expected from previous studies. Figure 4 shows the total vorticity $\omega = \hat{z} \times \boldsymbol{\nabla}\boldsymbol{u}$ in a single frame of measured data at $Re = 40$. Vorticity provides a concise and convenient description of quasi-two-dimensional flows. Apparent in the measured vorticity is an alternating pattern whose characteristic size matches the forcing scale $L_f = 25.4$ mm. The curl of the incompressible component in the same frame, $\omega_{\text{inc}} = \hat{z} \times \boldsymbol{\nabla}\boldsymbol{u}_{\text{inc}}$, is also shown in Fig. 4. The same large-scale spatial pattern apparent in the measured data appears again in the incompressible component, which
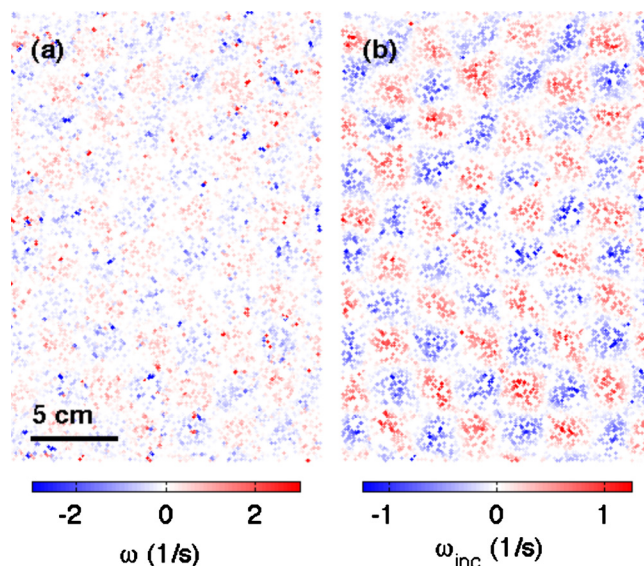

FIG. 4. (Color online) Example vorticity fields at $Re = 40$ for (a) ω and (b) ω_{inc}. As in Fig. 2, each tracked particle is represented by a dot; here color indicates vorticity. We avoid edge effects by considering only a subregion of the field of view of the camera. The vorticity of the incompressible component corrects outliers while preserving the spatial structure of the measured data.

accounts for the majority of the measured vorticity. The curl of the compressible component of the flow vanishes to within our numerical precision, as required by Eq. (4).

The measured in-plane divergence field $\Delta = \boldsymbol{\nabla} \cdot \boldsymbol{u}$ gives a direct indication of three-dimensionality in a flow. Figure 5 shows the divergence in the same single frame of data at $Re = 40$. Also shown is the divergence of the explicitly compressible component, $\Delta_{\text{comp}} = \boldsymbol{\nabla} \cdot \boldsymbol{u}_{\text{comp}}$. The divergence of the incompressible component is identically zero, as again required by Eq. (4).
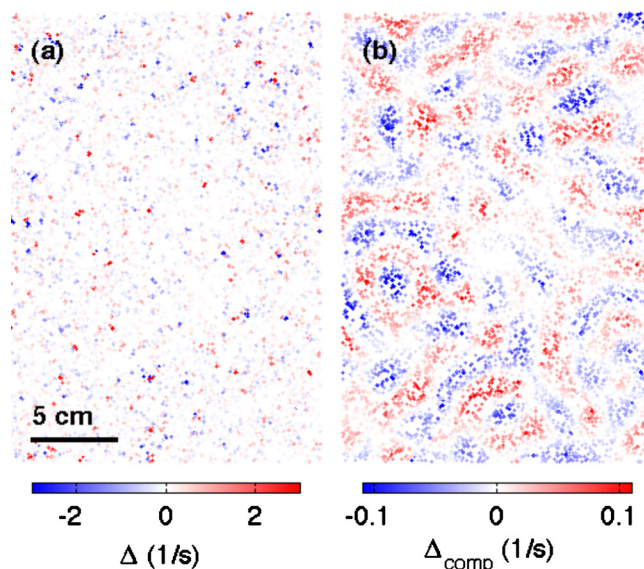

FIG. 5. (Color online) Example divergence fields at $Re = 40$, plotted in the same way the vorticity is plotted in Fig. 4, for (a) Δ and (b) Δ_{comp}. At low Reynolds number, the majority of the compressibility is due to outliers and does not project onto any basis mode ϕ_l.
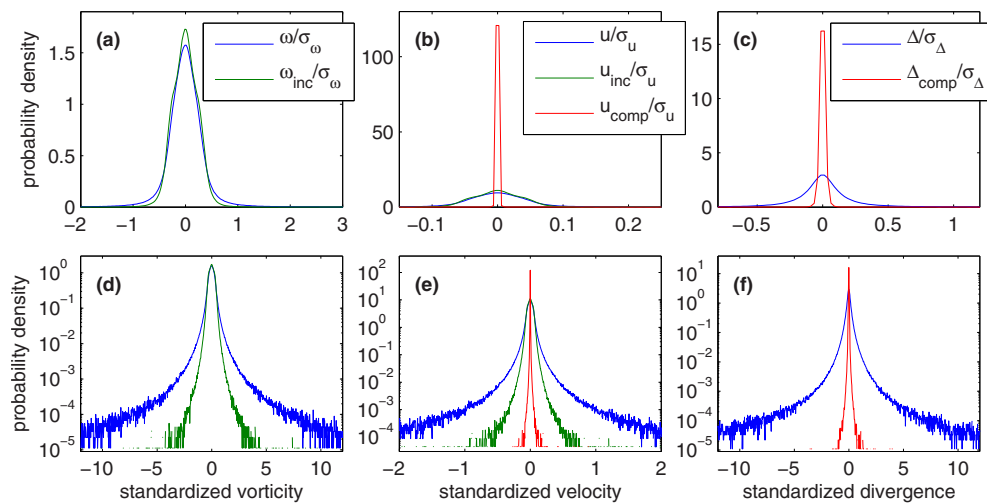
FIG. 6. (Color online) (a) Vorticity, (b) velocity, and (c) divergence PDFs at $Re=40$. The same plots are repeated on semilogarithmic axes with different horizontal scales in (d)–(f), respectively. Vorticity, velocity, and divergence plots are standardized using the standard deviation of the measured vorticity (σ_ω), velocity (σ_u), and divergence (σ_Δ), respectively. Each plot is constructed from all particles in the subregion shown in Fig. 4 over 400 frames (order 10^6 particles). At low Re, ω_{inc} and u_{inc} closely match ω and u. Although Δ has wide tails, the data do not project well onto the explicitly compressible component because Δ_{comp} is much more narrow. Together, these results suggest that three-dimensional effects are negligible at this Reynolds number.

Figures 4 and 5 show a small number of outlier particles whose measured vorticity and/or divergence are unusually large. Some of these outliers may be due to dust on the surface of the test fluid, which may be identified as a particle. However, most of the outliers visible in Figs. 4 and 5, as well as elsewhere in our data, are likely due to tracking errors. Some errors are unavoidable in particle tracking. Their number can be reduced with stringent software parameters, but only at a steep cost to the number of real tracks recorded. We therefore use tracking parameters that allow for the identification of more particles and more tracks, even if a few outliers persist, because those outliers can be easily corrected. With the parameters chosen for this study, about 60% of the image intensity maxima become part of a track at least ten frames long, which are the only tracks we retain.

In fact, outliers are automatically corrected by projecting data onto an appropriate basis. Because particles with erratically large velocities are rare, they make a statistically insignificant contribution [see Eq. (12)]. The results of projection are therefore dominated by the large number of measurements that are not outliers. The effect is evident by eye in the projected vorticity shown in Fig. 4. Because tracking individual particles produces data sets of high resolution, the removal of outliers can also be quantified by statistical measures, such as the probability density function (PDF) of ω at $Re=40$, shown in Fig. 6. Here, outliers lead to long tails in the vorticity distribution of the measured data. The PDF of ω_{inc} has much narrower tails, indicating that outliers have been eliminated.

Outside the tails, ω closely matches ω_{inc} (Fig. 6), consistent with single-frame observations like those shown in Fig. 4. At low Re, the measured flow is contained almost entirely in the incompressible component. The PDF of velocity, also shown in Fig. 6, supports this assertion. The measured velocity closely matches the incompressible component except at locations with unusually large velocity, which are in the tails of the distribution. The PDF of u_{comp} is

strongly peaked at zero and is typically much smaller than the PDF of either u or u_{inc}.

PDFs of the in-plane divergence, also shown in Fig. 6, give additional evidence that the flow is nearly two dimensions at $Re=40$. Although Δ is sharply peaked at zero and is therefore typically small, it has wide tails. The PDF of Δ_{comp}, however, is much more narrow and falls substantially below Δ at values away from zero, even though Δ_{comp} is the divergence of the component that may be explicitly compressible in the plane. These results together indicate that the measured data do not project well onto any compressible basis mode ϕ_l at this low Re: the measured divergence cannot be accounted for accurately by the explicitly nonsolenoidal flow component. Rather, the tails of the Δ distribution are due to outliers caused by tracking errors. Actual flow in the depth direction is very small at low Re.

Measurements made at increased Re, with stronger forcing, tell a different story. Figure 7 shows the vorticity of a single frame of measured data at $Re=230$. The flow field is clearly no longer pinned to the regular lattice of the magnet array but instead shows a complex spatial structure that dynamically evolves over time, as expected from previous studies. As before, there are outliers in the vorticity field due to tracking errors; comparing ω to ω_{inc} in Fig. 7, however, shows again that outliers are eliminated by projection, whereas the spatial structure of the flow is preserved. PDFs of the in-plane vorticity, velocity, and divergence at $Re=230$ are shown in Fig. 8. The separation between ω and ω_{inc} is larger than at lower Reynolds number, indicating that the flow is not modeled as well by its incompressible component alone. A flattening of the velocity PDFs also suggests out-of-plane motion. Such motion tends to evacuate tracer particles from vortex cores, causing those low-velocity regions to be poorly sampled.

In order to understand the evolution from low-Re flow that is nearly two-dimensional to high-Re flow that has a non-negligible out-of-plane component, we study the behav-
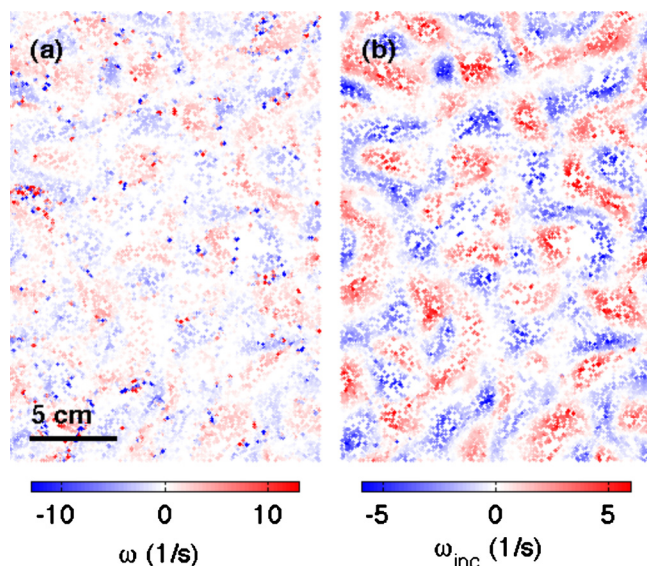
FIG. 7. (Color online) Example vorticity fields for (a) ω and (b) ω_{inc} at $Re=230$, plotted as in Fig. 4. At higher Re, the forcing lattice no longer dominates flow structure.

FIG. 9. (Color online) Variation of the root-mean-square velocity U with Re. U and U_{inc} have similar magnitude and increase smoothly with Re, whereas U_{comp} rises sharply at $Re_c=205$.

ior as a function of Re. Figure 9 shows the variation of root-mean-square velocity $U=\sqrt{\langle u^2 \rangle}$ with Re. The root-mean-square velocity of the incompressible flow component, U_{inc}, nearly matches U at each value of Re, indicating that nearly all of the measured flow is contained in the incompressible component. The root-mean-square velocity of the compressible component, U_{comp}, likewise increases linearly with Re, though with a smaller slope. Above a critical value Re_c, however, the slope of this increase abruptly steepens. For $Re<Re_c$, U_{comp} is well fit by a line that passes through the origin (i.e., $U_{comp}=0$ at $Re=0$). For $Re>Re_c$, however, the data are well fit by a line that does *not* pass through the origin. This result suggests that an instability is responsible for the stronger out-of-plane motions for $Re>Re_c$; we associate the weak rise of U_{comp} with Re below Re_c with un-
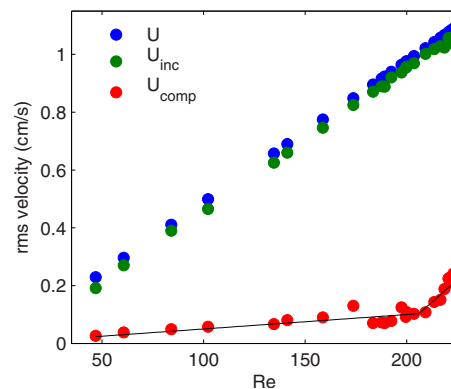
avoidable Ekman pumping, as discussed further below. We fit a piecewise linear function to the measurements, minimizing the squared error and leaving Re_c unconstrained. The resulting fit is shown in Fig. 9; it gives $Re_c=205$. Careful observation also shows that U_{inc} departs from U with a similar linear trend beginning near $Re=Re_c$.

The variation of root-mean-square vorticity and divergence with Re, shown in Fig. 10, is also consistent with an instability to three-dimensional flow at $Re=Re_c$. Like U_{comp}, the root-mean-square divergence shows an abrupt increase at $Re=Re_c$, both in the measured data and in the compressible component. The measured root-mean-square vorticity likewise shows a slow linear increase for $Re<Re_c$ and then a much more rapid rise at higher Re. This sharp increase in the vorticity is likely due to three-dimensional motion. The only source term in the vorticity equation is the vortex stretching term, which vanishes identically in purely two-dimensional flow (because in two-dimensional flow the vorticity must always be orthogonal to the rate of strain). The rapid increase of the vorticity we observe suggests that this source term is
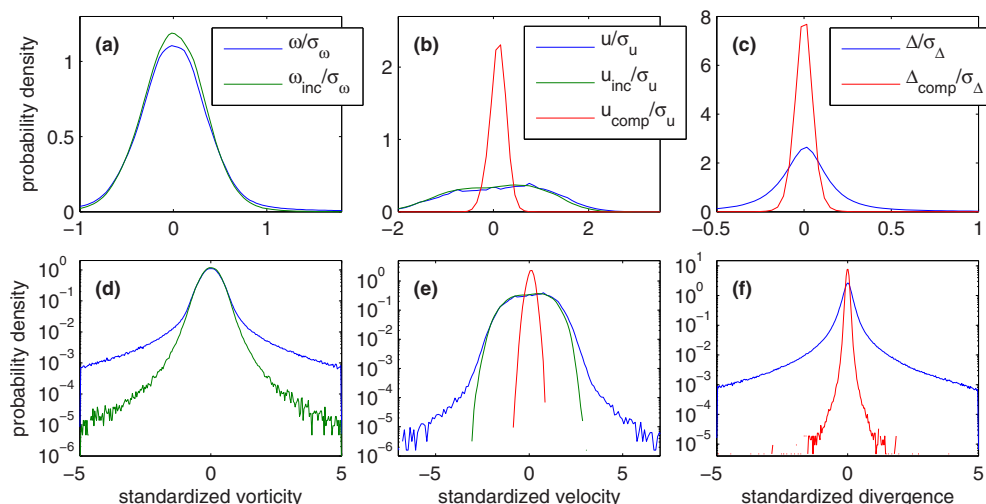

FIG. 8. (Color online) (a) Vorticity, (b) velocity, and (c) divergence PDFs at $Re=230$. The same plots are repeated on semilogarithmic axes with different horizontal scales in (d)–(f), respectively. Each plot is standardized as in Fig. 6 and is constructed from all particles in the subregion shown in Fig. 4 over 400 frames (order 10^6 particles). An increased separation between ω and ω_{inc}, along with flattening of the velocity PDFs, shows that three-dimensional effects have become appreciable.
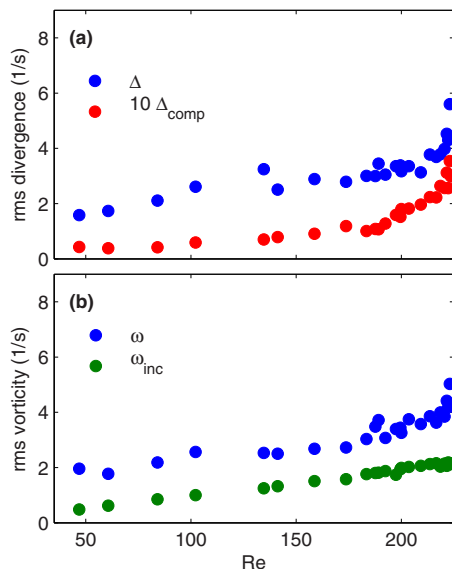
FIG. 10. (Color online) Variation of the root-mean-square (a) divergence and (b) vorticity with Re for the same data as in Fig. 9. Both quantities suggest the onset of stronger three-dimensional flow near Re_c, in agreement with measurements of the velocity (Fig. 9).

only present above Re_c, indicating that now vorticity is present with a component in the plane. This observation is borne out by visual inspection of the motion of particles in the flow. In Fig. 11, we show single snapshots of the tracer particles at $Re=40$ and 230. At the higher Reynolds number, particles appear to cluster on filamentary structures that rotate about in-plane axes and have larger out-of-plane velocities. In both cases the flow is dominated by its two-dimensional component, but the three-dimensional component is visibly stronger for $Re > Re_c$.
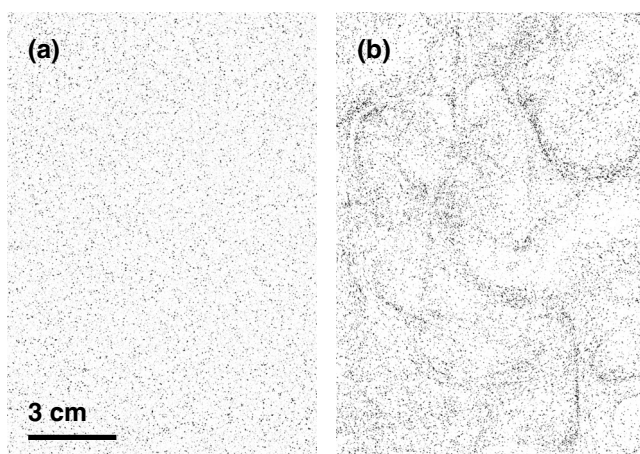

FIG. 11. Snapshots of tracer particles at (a) $Re=40$ and (b) $Re=230$. Whereas the particle density is nearly uniform at low Reynolds number, particles appear to cluster in filamentary regions at high Reynolds number. Those regions correspond to structures rotating about in-plane axes, with larger out-of-plane velocities, as can be observed directly in the corresponding movies.

V. DISCUSSION AND CONCLUSIONS

We have tracked particles to extract Lagrangian velocity measurements in an electromagnetically forced thin-layer flow of the sort commonly used to approximate two-dimensional fluid flow in the laboratory. By adapting a data processing technique from oceanography,[21] we separated the purely two-dimensional component of our measurements that is incompressible in the plane from the three-dimensional component that shows apparent compressibility. Examining the two components separately, we find that out-of-plane flow rises rapidly above a critical Reynolds number Re_c. In this section we will discuss the physical mechanisms responsible for the behavior we see.

One mechanism that produces out-of-plane motion in thin-layer flows is Ekman pumping,[13] an effect that is generic in rotating flows over a no-slip boundary. In a flow like ours, the electromagnetic forcing drives circulation in the plane. The top and bottom boundary conditions differ, however: the floor of the flow cell imposes a no-slip condition either directly[9] or through a lubricating layer[15] at the bottom of each vortex. Accordingly, vortices tend to rotate more slowly at their bottoms than at their tops, producing a vertical gradient in the centrifugal pressure gradient that drives a secondary vertical circulation.

This secondary Ekman flow, however, is not the result of an instability. Rather, it occurs at all Reynolds numbers and its magnitude is directly coupled to the vertical vorticity gradient. Thus, Ekman pumping cannot account for the abrupt increase in three-dimensionality that we observe at Re_c (Figs. 9 and 10). Instead, the Ekman pumping is the origin of the slow linear growth in U_{comp} for $Re < Re_c$. The stronger three-dimensionality that occurs only at increased Reynolds number must arise from a different mechanism.

One possibility for producing this stronger vertical flow is the presence of internal gravity waves[32] on the fluid/fluid interface in our apparatus. Internal waves can produce vertical motion in the bulk of a stratified fluid with an amplitude far in excess of any associated perturbations visible at the surface. In the ocean, for example, surface waves have typical amplitudes of order 1 m but internal waves on the pycnocline have typical amplitudes[32] of order 10 m. Nonlinear phenomena such as wave breaking or interaction occur only when wave amplitudes become large and thus could potentially account for the onset we observe. Previous studies of thin-layer flows have shown that stratification reduces out-of-plane motions[12,19] while suggesting that internal waves due to stratification may also cause the remaining three-dimensionality.[12] We have, however, observed similar three-dimensional effects as those shown here in flows with a single fluid layer, in which there is no stratification and therefore no internal waves. It is more likely that the abrupt increase of three-dimensionality we observe is due to a shear instability of the vertical velocity profile (which must vanish at the lower no-slip boundary). When the destabilizing effect of shear overcomes the viscous smoothing and stratification, vorticity with its axis in the plane may be generated, with associated three-dimensional flow.

By separating the measured velocity of each particle into

two- and three-dimensional components, we have introduced a new tool for quantifying three-dimensionality in shallow flows. Our experiments were performed at Reynolds numbers higher than in previous studies that reported good two-dimensionality[9,10] but lower than in previous studies finding poor two-dimensionality.[17–19] Thus, the presence of an onset in this regime provides a link between these previous reports. One open question is the relation between the arrays of vortices as considered here and monopolar vortices as examined in some previous studies[17–19] because vortex arrays may possibly suppress some three-dimensional motion. Another open question is the relation between steady forcing as considered here and decaying flow. Finally, we note that by using the projection technique described here and considering the purely two-dimensional component alone, future experimental explorations may also provide more accurate experimental approximations of two-dimensional flow than previously available even when three-dimensional effects are present.

ACKNOWLEDGMENTS

[1] R. H. Kraichnan, "Inertial ranges in two-dimensional turbulence," Phys. Fluids **10**, 1417 (1967).

[2] C. E. Leith, "Diffusion approximation for two-dimensional turbulence," Phys. Fluids **11**, 671 (1968).

[3] G. K. Batchelor, "Computation of the energy spectrum in homogeneous two-dimensional turbulence," Phys. Fluids **12**, II-233 (1969).

[4] A. E. Perry and M. S. Chong, "A description of eddying motions and flow patterns using critical-point concepts," Annu. Rev. Fluid Mech. **19**, 125 (1987).

[5] G. A. Voth, G. Haller, and J. P. Gollub, "Experimental measurements of stretching fields in fluid mixing," Phys. Rev. Lett. **88**, 254501 (2002).

[6] P. B. Rhines, "Geostrophic turbulence," Annu. Rev. Fluid Mech. **11**, 401 (1979).

[7] L. M. Smith, J. R. Chasnov, and F. Waleffe, "Crossover from two- to three-dimensional turbulence," Phys. Rev. Lett. **77**, 2467 (1996).

[8] P. Tabeling, S. Burkhart, O. Cardoso, and H. Willaime, "Experimental study of freely decaying two-dimensional turbulence," Phys. Rev. Lett. **67**, 3772 (1991).

[9] J. Paret, D. Marteau, O. Paireau, and P. Tabeling, "Are flows electromagnetically forced in thin stratified layers two dimensional?," Phys. Fluids **9**, 3102 (1997).

[10] B. Jüttner, D. Marteau, P. Tabeling, and A. Thess, "Numerical simulations of experiments on quasi-two-dimensional turbulence," Phys. Rev. E **55**, 5479 (1997).

[11] D. Rothstein, E. Henry, and J. P. Gollub, "Persistent patterns in transient chaotic fluid mixing," Nature (London) **401**, 770 (1999).

[12] M. P. Satijn, A. W. Cense, R. Verzicco, H. J. H. Clercx, and G. J. F. van Heijst, "Three-dimensional structure and decay properties of vortices in shallow fluid layers," Phys. Fluids **13**, 1932 (2001).

[13] T. H. Solomon and I. Mezić, "Uniform resonant chaotic mixing in fluid flows," Nature (London) **425**, 376 (2003).

[14] H. J. H. Clercx, G. J. F. van Heijst, and M. L. Zoeteweij, "Quasi-two-dimensional turbulence in shallow fluid layers: The role of bottom friction and fluid layer depth," Phys. Rev. E **67**, 066303 (2003).

[15] M. K. Rivera and R. E. Ecke, "Pair dispersion and doubling time statistics in two-dimensional turbulence," Phys. Rev. Lett. **95**, 194503 (2005).

[16] L. Rossi, J. C. Vassilicos, and Y. Hardalupas, "Electromagnetically controlled multi-scale flows," J. Fluid Mech. **558**, 207 (2006).

[17] R. A. D. Akkermans, A. R. Cieslik, L. P. J. Kamp, R. R. Trieling, H. J. H. Clercx, and G. J. F. van Heijst, "The three-dimensional structure of an electromagnetically generated dipolar vortex in a shallow fluid layer," Phys. Fluids **20**, 116601 (2008).

[18] R. A. D. Akkermans, L. P. J. Kamp, H. J. H. Clercx, and G. J. F. van Heijst, "Intrinsic three-dimensionality in electromagnetically driven shallow flows," EPL **83**, 24001 (2008).

[19] R. A. D. Akkermans, L. P. J. Kamp, H. J. H. Clercx, and G. J. F. van Heijst, "Three-dimensional flow in electromagnetically driven shallow two-layer fluids," Phys. Rev. E **82**, 026314 (2010).

[20] H. J. H. Clercx and G. J. F. van Heijst, "Two-dimensional Navier–Stokes turbulence in bounded domains," Appl. Mech. Rev. **62**, 020802 (2009).

[21] F. Lekien, C. Coulliette, R. Bank, and J. Marsden, "Open-boundary modal analysis: Interpolation, extrapolation, and filtering," J. Geophys. Res. **109**, C12004 (2004).

[22] D. H. Kelley and N. T. Ouellette, "Using particle tracking to measure flow instabilities in an undergraduate laboratory experiment," Am. J. Phys. **79**, 267 (2011).

[23] D. Vella and L. Mahadevan, "The 'Cheerios effect'," Am. J. Phys. **73**, 817 (2005).

[24] N. T. Ouellette, P. J. J. O'Malley, and J. P. Gollub, "Transport of finite-sized particles in chaotic flow," Phys. Rev. Lett. **101**, 174504 (2008).

[25] N. T. Ouellette, H. Xu, and E. Bodenschatz, "A quantitative study of three-dimensional Lagrangian particle tracking algorithms," Exp. Fluids **40**, 301 (2006).

[26] F. Toschi and E. Bodenschatz, "Lagrangian properties of particles in turbulence," Annu. Rev. Fluid Mech. **41**, 375 (2009).

[27] N. Mordant, A. M. Crawford, and E. Bodenschatz, "Experimental Lagrangian acceleration probability density function measurement," Physica D **193**, 245 (2004).

[28] N. T. Ouellette, H. Xu, and E. Bodenschatz, in *Springer Handbook of Experimental Fluid Mechanics*, edited by C. Tropea, A. L. Yarin, and J. F. Foss (Springer-Verlag, Berlin, 2007).

[29] G. B. Arfken and H. J. Weber, *Mathematical Methods for Physicists*, 5th ed. (Harcourt Academic, San Diego, 2001).

[30] P. Lynch, "Partitioning the wind in a limited domain," Mon. Weather Rev. **117**, 1492 (1989).

[31] W. H. Press, S. A. Teukolsky, W. T. Vetterling, and B. P. Flannery, *Numerical Recipes: The Art of Scientific Computing*, 3rd ed. (Cambridge University Press, London, 2007).

[32] C. Garrett and W. Munk, "Internal waves in the ocean," Annu. Rev. Fluid Mech. **11**, 339 (1979).